A micro-scale insight into a back-arc trans-crustal plumbing system: The case of Marsili volcano, Southern Tyrrhenian Sea

Fabio Colle [a,*], Matteo Masotta [b,c], Simone Costa [d], Pier Paolo Giacomoni [b], Teresa Trua [a,e], Michael Marani [e]

[a] *Dipartimento di Scienze Chimiche, della Vita e della Sostenibilità Ambientale (SCVSA), Plesso Geologico, University of Parma, Italy*
[b] *Dipartimento di Scienze della Terra, University of Pisa, via S. Maria 53, 56126 Pisa, Italy*
[c] *CISUP, Centro per la Integrazione della Strumentazione dell'Università di Pisa, Lungarno Pacinotti, Pisa, Italy*
[d] *Istituto Nazionale di Geofisica e Vulcanologia, Sezione di Pisa, Via Cesare Battisti, 53, 56125 Pisa, Italy*
[e] *Istituto di Scienze Marine (ISMAR), Consiglio Nazionale delle Ricerche (CNR), Via Gobetti 101, 40129 Bologna, Italy*

ABSTRACT

The Marsili seamount is a submarine volcano in the Tyrrhenian Sea that originated in a back-arc setting. Aiming to define the complexity of its trans-crustal plumbing system, we explored the compositional and textural variations of crystal cargoes in basaltic to andesitic lavas collected from three different sectors of the volcano (northern, axial, and lateral). Lavas collected from the northern sector are basaltic in composition and contain minerals with a narrow and more primitive composition compared to basalt and basaltic andesitic lavas sampled at the lateral and axial sectors, hosting a crystal cargo characterized by a broader chemical variability. Crystal-poor andesitic lavas were only collected at the axial summit sector of the volcano. Glomerocrysts with diverse mineralogy are ubiquitous in lavas erupted from all sectors and testify to the presence of crystal mush domains in the whole trans-crustal system. Thermobarometric calculations performed on clinopyroxene coupled to mass-balance and thermodynamic modeling collectively point to a polybaric and spatially heterogeneous plumbing system. The relatively less differentiated basaltic magmas erupted in the northern and axial sectors reside at depth corresponding to the lower crust-mantle boundary (300–450 MPa, 1040–1080 °C). Basaltic and basaltic andesitic magmas extracted from this deep storage zone formed, over time, scattered magma storage zones in the 10–12 km-thick oceanic crust beneath the Marsili volcano. The shallower magma storage zones sourced the andesitic magmas (<250 MPa, 920–980 °C) erupted in the axial summit sector. In turn, basaltic and basaltic andesitic magmas erupted in the lateral sector testify to intermediate storage conditions (200–400 MPa, 980–1060 °C) and variable degree of evolution. The variable content of incompatible (^{T}Al and Ti) and REE in clinopyroxene contained in basaltic lavas from the three sectors relates to different degrees of undercooling (ΔT), with magmas erupted from the northern sector recording higher undercooling ($\Delta T = 90 \pm 39$ °C) compared to those erupted from the lateral ($\Delta T = 52 \pm 27$ °C) and axial ($\Delta T = 30 \pm 25$ °C) sectors. The emerging scenario is that basaltic magmas erupted from the northern sector experienced a more rapid ascent (also testified by the occurrence of high-Fo olivine and dendritic clinopyroxene in the groundmass) compared to magmas erupted at the lateral and axial sectors, otherwise experiencing prolonged residence within the crust.

1. Introduction

Defining the structure of magmatic systems feeding active volcanoes is a crucial step for the understanding of magma dynamics and pathways in the crust, which yields substantial implications for the management of volcanic hazard (Burchardt et al., 2022). The concept of "trans-crustal" plumbing system models, characterized by complex interactions between ascending magmas and crystal- and melt- rich zones (e.g., Cashman et al., 2017), stresses the importance of integrating whole-rock and mineral chemistry data with the petrographic information. This approach has been found to be fundamental for deciphering the complexity of magmatic processes and to obtain a broader view of volcanic plumbing systems, unveiling their variability through time and space (Bennet et al., 2019; Burns et al., 2022; Giacomoni et al., 2014;

Lormand et al., 2021; Mollo et al., 2022; Ubide et al., 2019b). While the crystal cargo of a single eruption provides a snapshot of magma dynamics relative to a part of the reservoir, a complete picture of the physico-chemical conditions and magma pathways through the plumbing system can be obtained only from the integrated study of multiple eruptive events (Boschetty et al., 2022; Geiger et al., 2018; Jerram et al., 2018; Kahl et al., 2015; Weber et al., 2020). The comprehensive analysis of eruptive products representative of distinct domains of a volcanic system is particularly relevant in the case of submarine volcanoes, owing to the obvious limitations in terms of sampling and surface observation.

Here we present the case of Marsili seamount, a large (70 km long, 20 km wide) submerged volcano located in the Tyrrhenian Sea, originated in a back-arc setting and characterized by a plumbing system that extends across the entire oceanic crust (Marani and Trua, 2002). Marine campaigns targeting Marsili volcano (MV) collected a large number of samples from three different sectors of the volcano: the axial, the northern and the lateral sector (Fig. 1; Gamberi et al., 2006; Marani et al., 1999). Previous petrological studies carried out on sets of MV lava samples revealed remarkable differences, in terms of phenocrysts proportions, chemical composition and zoning, among the basalt and basaltic andesitic magmas, providing evidence for a wide spectrum of petrogenetic processes (Albert et al., 2022; Trua et al., 2010, 2011, 2014, 2018; Trua and Marani, 2021). This petrologic diversity is linked to the complexity of the MV trans-crustal plumbing system, providing

Fig. 1. Sketch showing the location of Marsili Basin (MB) in the Southern Tyrrhenian Sea (inset) and bathymetric map of Marsili volcano (MV) showing sample location. The inset shows the locations of the Marsili Basin (MB; red boxed area), the Vavilov Basin (VB), the Aeolian volcanic arc (AVA), and the Ionian Oceanic Plate (IOP). The three different sectors of the MV have been highlighted with colored squares (purple, blue and orange for northern sector, axial sector and lateral sector, respectively). MV sampling sites (grey dots) and classification of the volcanic samples from Trua et al. (2011). The sampling sites investigated in this study are represented by dots filled with the respective sector color. (For interpretation of the references to color in this figure legend, the reader is referred to the web version of this article.)

evidence of changes in magma dynamics and reservoir architecture that cannot be inferred using the sole whole-rock geochemistry. Moreover, while previous studies were generally focused on the analysis of a single mineral phase, a comparative analysis of the crystal cargoes variability in the erupted magmas is lacking. Hence, a more general perspective which considers the effects of different pathways on the magmatic evolution and the petrological heterogeneity of the MV feeding system has yet to be gained.

In this study, we investigated the crystal cargoes of selected basaltic to andesitic lava samples collected from the three sectors of the MV with the aim of improving our understanding of magmatic evolution and transfer across the trans-crustal plumbing system. In particular, we combine the chemical database obtained from the revision of the existing MV petro-chemical data (Albert et al., 2022; Trua et al., 2014, 2018; Trua and Marani, 2021) with the new textural and mineral chemistry data. The whole chemical database is employed to perform thermobarometric calculations as well as for mass-balance differentiation modeling and thermodynamic simulations. The assessment of the physico-chemical conditions controlling the magmatic evolution across the complex trans-crustal plumbing system allows to establish a link between the petrologic variability of the eruptive products and the dynamics of magmas erupted at the different MV sectors. This comprehensive picture may have fundamental implications for assessing the impact of possible eruptions from the different sectors on the stability of the MV edifice and the consequent hazard assessment for landslide-induced tsunami along the Tyrrhenian coasts (e.g., Gallotti et al., 2021). The acquired knowledge may also help in the identification of the nature of magmatic processes in back-arc submarine volcanoes elsewhere (e.g.: Beier et al., 2015; Jeanvoine et al., 2021).

2. Geological context and petrological background

The Tyrrhenian Sea is a complex back-arc basin, associated with the tectonic history resulting from the convergence of the African and the Eurasian plates (Zitellini et al., 2019 and references therein). It represents one of the few modern marine back-arc basins that initiated in continental lithosphere (Vasey et al., 2021). The most recent spreading volcanic activity of the Tyrrhenian back-arc area is expressed by the MV, an active (< 0.7 Ma) submarine stratovolcano, roughly aligned NNE-SSW, that rises from 3500 m to 500 m below sea level at the spreading center of the Marsili Basin (Marani and Trua, 2002), the latter located at the southern portion of the Tyrrhenian Sea (Fig. 1). Geophysical investigations indicate an oceanic nature for the crust underlying the Marsili Basin, identifying the Moho at a relatively shallow depth of 10–12 Km (Manu-Marfo et al., 2019).

Geochemical studies carried out on a selection of the sampled lavas have shown that the MV predominantly erupted basaltic and basaltic andesitic magmas, while a minor volume of andesitic products erupted at the axial summit zone (Trua et al., 2002, 2007, 2011). The more recent products with a geochronological constraint (2-3 ka) are instead represented by trachytic tephra (Gennaro et al., 2023; Iezzi et al., 2014, 2020; Tamburrino et al., 2015) found on a small volcanic cone located in a landform where, based on geomorphological data, the younger activity of MV developed (Nicotra et al., 2024).

The MV lavas have a calc-alkaline affinity, like the one shown by the igneous rocks that paved the Marsili Basin oceanic crust (Kastens and Mascle, 1990). Geochemical and isotopic data suggest that the primary magmas derive from melting of a subduction-metasomatized mantle wedge environment, mixed with an enriched, African-derived mantle component (Trua et al., 2010, 2011). In turn, whole-rock data from basaltic to andesitic lava samples are indicative of fractional crystallization processes, with no involvement of assimilation of continental crust (Trua et al., 2002, 2007, 2011).

Previous petrological studies on lavas collected from MV used diverse mineral-liquid equilibria models and thermodynamic simulations, providing the following estimates of the pre-eruptive conditions:
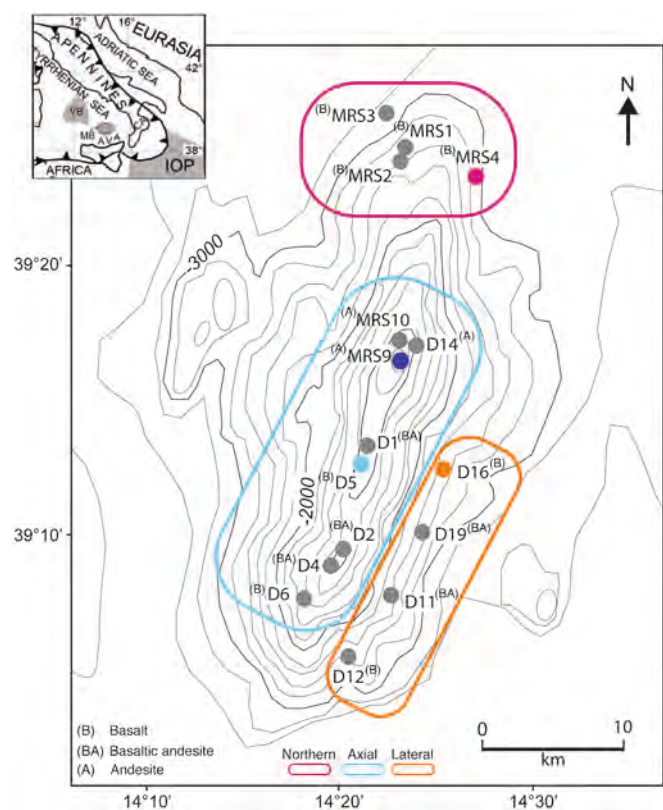
temperatures varying from 1050 to 1170 °C, pressures varying from 20 to 500 MPa, oxygen fugacity conditions ranging from −0.6 to +2.5 log units above the NNO oxygen buffer and melt-H_2O content in the range of 0.5–5 wt% (Trua et al., 2014, 2018; Trua and Marani, 2021). The variety of textures and compositions observed for olivine (Albert et al., 2022), clinopyroxene (Trua and Marani, 2021) and plagioclase (Trua et al., 2018) crystals points to petrological differences existing among individual lava samples. Altogether, these mineral studies provide evidence for the following magmatic scenarios: i) mantle melts injected at crust-mantle transition depths cool and crystalize, forming a deep, clinopyroxene-dominated crystal mush; ii) the extraction of basic magmas appears to be more rapid in the northern sector than in the other portions of the volcanic edifice; iii) some chemically evolved melts rapidly rising from the deeper zones and briefly stalling at shallower crustal levels give rise to the crystal-poor andesitic lavas; iv) locally, magmatic inputs from the deeper zones may intercept and mix with shallower magma bodies with different composition, thus generating hybrid basic magmas.

3. Sample and methods

3.1. Sample selection and preparation

The extensive collection of lava samples dredged from the MV during the MAR98 and TIR2000 cruises executed by the CNR ship R/V Urania (Gamberi et al., 2006; Marani et al., 1999) is permanently stored at the ISMAR-CNR repository (http://www.ismar.cnr.it/infrastructures/core-repository). Four MV lava samples were selected for a detailed petrochemical investigation: three are basaltic samples, dredged at the northern (MRS4), axial (D5), and lateral (D16) sectors of the MV; one is an andesitic sample (MRS9) from the axial summit zone (Fig. 1). Whole-rock compositions of the MV lavas are from Trua et al. (2011) (Table EA1). In order to provide a more robust insight on the crystallization conditions associated to these different sectors of the MV edifice, we also revised the petrography and mineral chemistry of other existing lava samples (Albert et al., 2022; Trua et al., 2002, 2014, 2018; Trua and Marani, 2021). These further samples were collected from the northern sector (MRS1, MRS2, and MRS3 basaltic samples), the axial sector (D6 basaltic sample; D1, D2, and D4 basaltic andesitic samples), the axial summit zone (D14 and MRS10 andesitic samples), and along the lateral sector (D12 basaltic sample; D11 and D19 basaltic andesitic samples) of the volcanic edifice (Fig. 1).

Thin sections of the selected samples were prepared from small blocks of the original samples and investigated using a petrographic microscope. The free software package ImageJ was used for measuring crystal size (major axis of the best fitting ellipse; see Pontesilli et al., 2019), phenocryst abundance and vesiculation. The remaining aliquots of the blocks (8–10 g) were cleaned from any external sign of alteration and used to make a glass for major and trace element analysis (Table EA1). Each sample block was crushed using an agate mortar to make a powder and melted at 1400 °C for 1 h in a Fe-presaturated Pt crucible, using a high temperature furnace Nabertherm LH7 01/17 installed at the HP-HT laboratory of the Dipartimento di Scienze della Terra, at the University of Pisa (Italy). The crucible was quenched in deionized water and the homogeneity of the glass inspected under petrographic microscope.

3.2. Analytical methods

Polished thin sections were studied by back scattered electron (BSE) imaging and energy dispersive X-ray spectroscopy (EDS) microanalysis using a field emission-scanning electron microscope (SEM) FEI Quanta 450 equipped with a Bruker QUANTAX XFlash Detector 6/10 at the Centro per la Integrazione della Strumentazione della Università di Pisa (CISUP). Microchemical data on minerals and glasses were determined by electron probe micro-analyzer (EPMA) using a JEOL JAX8600 at the Department of Earth Sciences of Florence. The analytical conditions were 15 kV of accelerating voltage with 20 nA of beam current and 3 μm beam size for olivine, pyroxene, and oxide and 10 nA beam current and 5 μm beam size for plagioclase. The counting time was 15 s on peak and 7 s in the background for major elements (except for the Na, counting 10 s on peak and 5 s in the background). For minor elements (P, Ni, Cr), counting times varied between 30 and 40 s on peak and between 15 and 20 s on the background. The primary standards used for calibration were albite Astimex for Si and Na, plagioclase Astimex for Al, olivine Astimex for Mg, diopside Asimex for Ca, sanidine Astimex for K, ilmenite Smithsonian for Ti and Fe, apatite Astimex for P, and barite Astimex for Ba and celestite Astimex for Sr.

Trace element analyses were carried out on glasses obtained by melting the natural rock powders and clinopyroxene crystals. Analyses were performed with the laser ablation-inductively coupled plasma-mass spectrometry (LA-ICP-MS) system installed at the Centre for Instrument Sharing of University of Pisa (CISUP), composed by an Elemental Scientific NWR-193 (Ar—F) excimer laser equipped with a TwoVol2 two-volume cell coupled with a PerkinElmer NexION 2000 ICP-MS. The laser was operated at a repetition rate of 10 Hz, using a spot size of 35 μm and a fluence of 4.6 J/cm². Signals were acquired for 30 s during ablation and 50 s with laser off (background). The synthetic glass standard NIST612 was used for tuning of the ICP-MS and as calibration standard, whereas the synthetic glass standard NIST610 and an in-house glass standard (BE-N) were used as quality monitor. Standard glasses were measured every 6-8 spots. Ca and Si concentrations (previously measured by EPMA) were used as internal standard for clinopyroxene and glass analyses, respectively. Accuracy and precision were better than 5% for all elements, except for Zn, which had an accuracy of 9% and a precision of 12%. Limits of detection were calculated according to Howell et al. (2013). Data processing was conducted using the commercial software Iolite v4 (Paton et al., 2011; Woodhead et al., 2007).

4. Results

4.1. Petrography

The four investigated lava samples are weakly to moderately porphyritic, with phenocrysts content ranging from 15 to 30 area% in the basaltic lavas and of 10 area% in the andesitic lava (Fig. 2). Phenocrysts occur both as isolated euhedral to subhedral crystals and in glomerocrysts (monomineralic or polymineralic). Olivine, clinopyroxene, and plagioclase are phenocryst phases in the basalts, whereas the dominant phenocryst phase in the andesite is plagioclase, followed by clinopyroxene and spinel (Fig. 2). Notably, spinel is absent as phenocryst in the basalts, but it occurs as microlite in the groundmass and as inclusion in olivine phenocrysts. Neither orthopyroxene nor amphibole were observed in the investigated samples, but these minerals were found in two andesitic samples (MRS10 and D14) and in a basaltic andesitic sample (D2) collected in the axial sector of MV (Trua et al., 2014). In the basaltic samples, the groundmass is microcrystalline and varies in texture from intergranular to intersertal, while it is pilotaxitic in the andesitic sample (Fig. 3). A slightly different groundmass texture was observed for a basalt from the northern sector (sample MRS1, studied more in detail in Trua et al., 2002), characterized by skeletal microcrysts of plagioclase (<200 μm) and acicular-dendritic microlites of clinopyroxene (<50 μm) (Fig. 3a) and suggesting a rapid cooling of the host magma. All the investigated lava samples exhibit a vesicular texture (Fig. 2). The degree of vesiculation is higher in the basalt from the axial sector (sample D5, 30 area%) and lower in the basalts from the north and lateral sectors (sample MRS4, 15 area%; sample D16, 10 area%). The andesite sample is moderately vesiculated (sample MRS9, 10 area%). The MRS4 basaltic sample from the northern sector exhibits spherical and pipe vesicles that are partly, or entirely, filled by a dark vesicular glass (Fig. 2a), resembling segregation structures observed in pillow lavas (Merle et al., 2005).
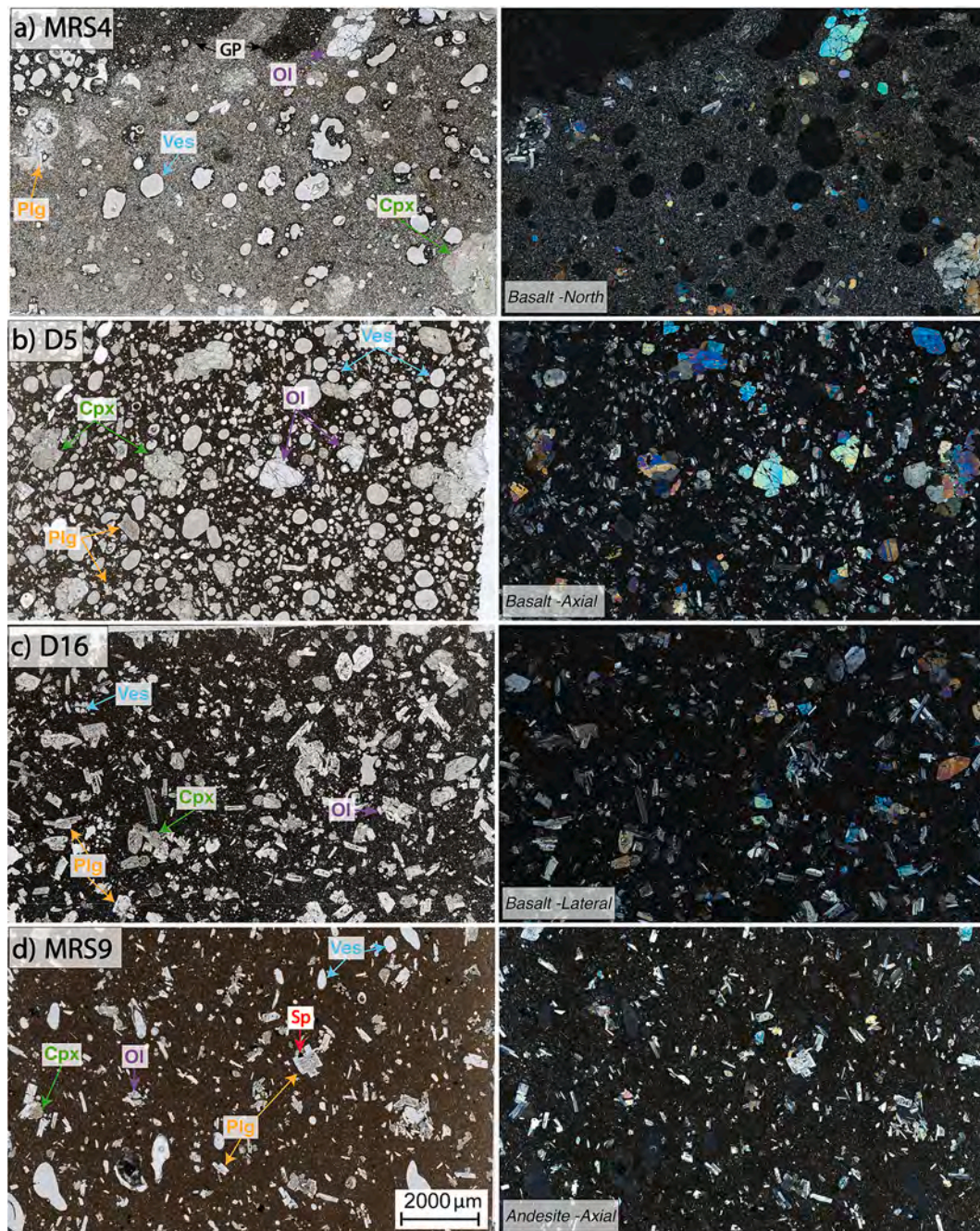
Fig. 2. Representative thin section photomicrographs in plane-polarized light (left column) and cross-polarized light (right column). (a) The basaltic sample MRS4 from the northern sector is characterized by a low porphyritic (PI = 15%) vesiculated texture and a phenocrysts assemblage composed by abundant olivine (Ol) and clinopyroxene (Cpx), and scarce plagioclase (Pl); note the presence of glassy pipes (GP). (b) The basaltic sample D5 from the axial sector is characterized by a vesiculated and more porphyritic (PI = 30%) texture compared to basalt MRS4, with a phenocryst assemblage composed by olivine, clinopyroxene and plagioclase. (c) The basaltic sample D16 from the lateral sector is characterized by a porphyritic texture (PI = 25%) and a mineral assemblage composed by olivine, clinopyroxene and plagioclase. The andesitic sample MRS9 from the axial sector is characterized by porphyritic texture (PI = 10%) and a phenocryst assemblage composed by plagioclase and minor amount of clinopyroxene, olivine and spinel (Sp). Note that the scale is the same for all the images.

Glomerocrysts (500–1000 μm in size) occur in all the basaltic and basaltic andesitic lavas examined in this study and their mineral assemblage varies sensibly with the provenance. In particular, glomerocrysts in basaltic lavas from the northern sector are either ultramafic (olivine+pyroxene) or gabbroic (pyroxene+plagioclase) in composition, whereas glomerocrysts in basalts and basaltic andesites from the axial and lateral sectors display a larger variability, being dominantly gabbroic (pyroxene+plagioclase).

These petrographic observations reinforce results from previous studies (Albert et al., 2022; Trua et al., 2002, 2018; Trua and Marani, 2021). As documented in these studies, basaltic lavas from the northern sector are generally characterized by a lower phenocryst content (10–15 area%) compared to basaltic and basaltic andesitic lavas from the lateral sector (20–25 area%) and the axial sector (25–30 area%). Relevant differences are also observed among these lavas, in terms of mineral assemblage and chemistry.
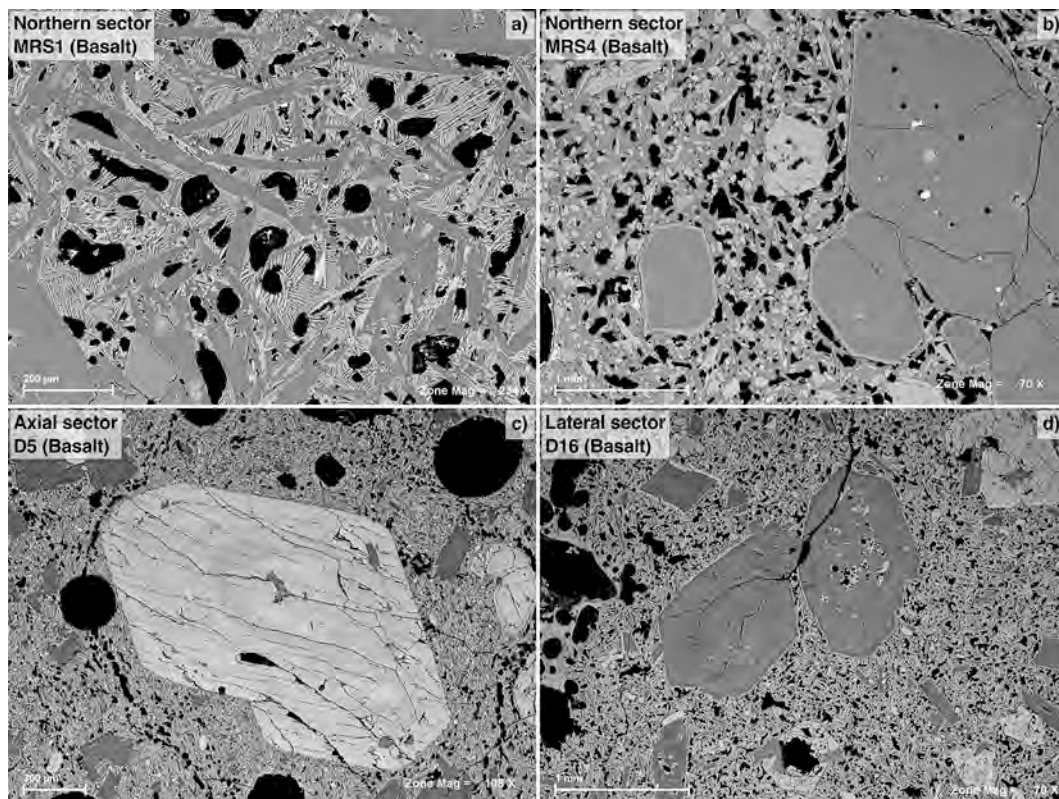
Fig. 3. Representative backscattered electron (BSE) images of investigated samples. (a) skeletal microcrysts (<200 μm) of plagioclase and acicular-dendritic microlites (<50 μm) of clinopyroxene in basalt MRS1 from the northern sector; (b) euhedral olivine phenocrysts in basalt MRS4, characterized by a narrow (<40 μm) rim with high BSE intensity and enclosing glassy, or partially crystallized, melt inclusions and micrometric spinel crystals; (c) clinopyroxene phenocrysts in basalt D5 from the axial sector showing concentric compositional zoning; (d) plagioclase phenocrysts in basalt D16 from the lateral sector, showing partially resorbed (sieve-textured) core, oscillatory zoning and euhedral overgrowth rims.

4.1.1. Olivine

Olivine phenocrysts are euhedral in all the basaltic studied samples and range in size from 100 to 800 μm. They often enclose brownish glassy, or partially crystallized, melt inclusions and micrometric spinel crystals (Fig. 3b). Olivine crystals contained in lavas from the northern sector are unzoned and show a sharp narrow (<40 μm) rim with higher BSE intensity (Fig. 3b). In contrast, basaltic lavas from the two other sectors contain olivine crystals characterized by normal zoning (Table EA2). In the andesitic samples, olivine is rare (three phenocrysts) and characterized by the absence of compositional zoning (Table EA2).

4.1.2. Clinopyroxene

Clinopyroxene crystals in basaltic samples are generally euhedral and range in size from 300 μm to 1000 μm. They often enclose crystals of olivine and plagioclase, and melt inclusions. While clinopyroxene contained in the basaltic lava from the northern sector appear compositionally homogeneous or sometimes characterized by hourglass sector zoning, clinopyroxene crystals contained in basaltic magmas erupted from the axial and lateral sectors display a manifest concentric zoning (Fig. 3c). In the andesitic sample, clinopyroxene is euhedral and ranges in size from 100 μm to 400 μm, chemical zoning is frequent, as also inclusions of opaque minerals.

4.1.3. Plagioclase

Plagioclase in basaltic samples from the axial and lateral sectors is mostly euhedral to subhedral and ranges in size from 200 to 1500 μm. Most of the crystals are characterized by partially resorbed cores (sieve texture) and oscillatory zoning, with euhedral overgrowth rims (Fig. 3d). Notably, sieve textures are less frequent in plagioclase phenocrysts from the northern sector.

4.2. Mineral chemistry

The chemical composition of mineral phases analyzed in the MV products from the northern, axial and lateral sectors are largely consistent with chemical data from previous works (Albert et al., 2022; Trua et al., 2002, 2014, 2018; Trua and Marani, 2021). New analyses from this study expand the existing data set and allow to recognize further compositional variability of the mineral phases related with the sector of provenance.

4.2.1. Olivine

Olivine crystals contained in basaltic lavas emitted from the northern sector (MRS1, MRS2, MRS3 and MRS4) are characterized by a relatively high values of forsterite (Fo_{82-90}) and CaO content (0.20–0.35 wt%) (Fig. 4; Table EA2). Basaltic and basaltic andesitic lavas from the axial sector (D1, D2, D4, D5 and D6) generally feature less primitive olivine crystals, characterized by a broader range of forsterite (Fo_{72-88}) and slightly lower CaO content (0.10–0.27 wt%) (Fig. 4; Table EA2). In contrast, the andesitic lava sample (MRS9) erupted from the same sector exhibits olivine crystals with lower forsterite (Fo_{70-71}) and CaO content (0.13–0.18 wt%) (Fig. 4; Table EA2). Olivine crystals contained in the four samples erupted from the lateral sector are characterized by different chemical compositions, with the basaltic and basaltic andesitic samples D11, D12 and D19 being more forsteritic (Fo_{80-88}) and with lower CaO content (0.10–0.25 wt%) compared to the basaltic sample D16, having lower forsterite (Fo_{63-85}) and higher CaO content (0.12–0.40 wt%) (Fig. 4; Table EA2).

4.2.2. Clinopyroxene

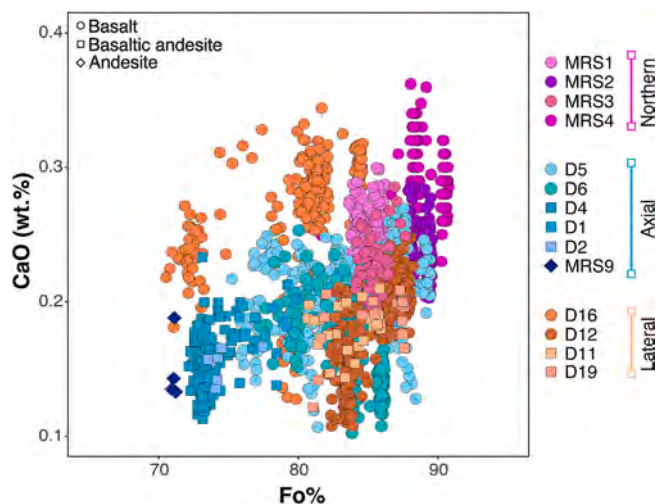Clinopyroxene crystals have been categorized according to the

Fig. 4. Compositional diagram showing CaO versus Fo content variation in olivine crystals. Basalt, basaltic andesite and andesite are reported as circle, square and diamond symbols, respectively. The color tone indicates the sector of provenance: purple for northern sector, blue for axial sector and orange for the lateral sector. (For interpretation of the references to color in this figure legend, the reader is referred to the web version of this article.)

classification scheme of Morimoto (1988) and are dominantly diopsidic in composition for samples from the northern sector and vary between diopsidic and augitic for samples from the axial and lateral sectors (Fig. 5; Table EA3a). In detail, the composition of clinopyroxene crystals in basaltic lavas emitted from the northern sector (MRS2, MRS4) is $Wo_{43-48}En_{42-50}Fs_{05-11}$, with Mg-number [Mg# = molar $100*Mg/(Mg + Fe^{2+})$ where Fe^{2+} is expressed as total iron] varying from 80 to 90. Overall, we note that the Mg# correlates inversely with TiO_2 (0.76–0.28 wt%) (Table EA3a; Fig. SM1). A broader compositional variability is observed for clinopyroxene crystals contained in basaltic and basaltic andesitic lavas erupted from the axial sector (D1, D2, D4, D5 and D6), characterized by composition ranging from diopside to augite ($Wo_{40-48}En_{41-49}Fs_{6-14}$) and Mg# ranging from 72 to 91 (Fig. 5; Table EA3a). The content of TiO_2 decrease from 1.60 to 0.19 wt% with increasing Mg# (Fig. SM1). The three andesitic samples from the same sector (MRS9, MRS10 and D14) are augitic in composition ($Wo_{37-45}En_{40-49}Fs_{11-17}$) and with Mg# ranging from 72 to 79 (Fig. 5). They show inverse correlation with TiO_2, which content varies from 1.27 to 0.43 wt% (Table EA3a; Fig. SM1). The lavas erupted from the lateral sector (D11,

D16 and D19) feature clinopyroxene crystals with composition varying from diopside to augite ($Wo_{35-48}En_{40-51}Fs_{05-17}$) and have Mg# ranging from 70 to 91 (Fig. 5; Table EA3a). The content TiO_2 varies from 1.76 to 0.17 wt% and shows an inverse correlation with the Mg# (Table EA3a; Fig. SM1).

Clinopyroxene crystals contained in the basaltic samples from the three sectors of MV were analyzed for the trace element content (Table EA3b). The basalt sampled in the northern sector is characterized by clinopyroxene crystals with generally higher REE content compared to basalts from the lateral and axial sector (Fig. 6). In turn, the axial sector is characterized by the clinopyroxene population with the largest variability of REE concentration.

4.2.3. Plagioclase

Plagioclase crystals have been classified following the Ab-An-Or ternary diagram and overall range from andesine to anorthite, with lavas from the axial sector showing a broader compositional variation of plagioclase compared to lavas from the northern and lateral sectors (Fig. 7; Table EA4).

Plagioclase contained in the basaltic lavas erupted from the northern sector (MRS1, MRS2, MRS3 and MRS4) is characterized by a range of composition varying from An_{66} to An_{93}. Basaltic and basaltic andesitic lavas from the lateral sector (D11, D12, D16 and D19) exhibit a slightly wider range of compositions, varying from An_{55} to An_{95}. A much broader range of anorthite content, varying from An_{32} to An_{92}, is instead observed for plagioclase contained in basaltic lavas erupted in the axial sector (D1, D2, D4, D5 and D6). Plagioclase crystals contained in the three andesitic samples (D14, MRS9 and MRS10) define a range in the An composition, varying from An_{47} to An_{90}, that overlap that of plagioclase contained in basaltic and basaltic andesitic samples. It is worth noting that two distinct populations of plagioclase compositions are observed for the basaltic andesitic sample D2 (An_{32-49} and An_{50-90}), and for the andesitic sample D14 (An_{50-67} and An_{84-91}) (Table EA4).

4.2.4. Spinel

Spinel crystals are not observed in all samples and, when present, they mainly consist of Cr-spinel enclosed in olivine crystals (Table EA5); titanomagnetite is found as well-developed small phenocrystals only in the andesitic samples. Notably, no substantial differences are noted among spinel crystals in lavas erupted from different sectors of the volcano.
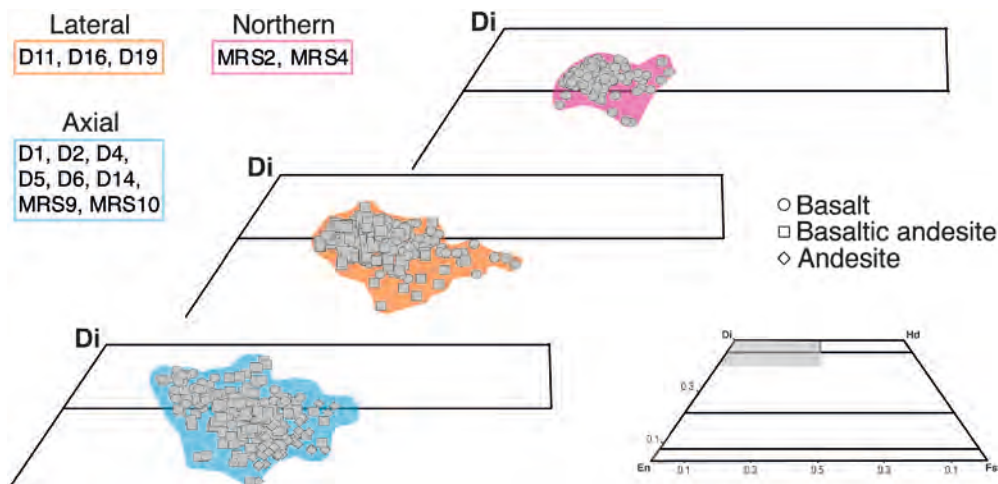

Fig. 5. Ternary diagram En-Wo-Fs (classification scheme of Morimoto, 1988) showing the compositional variability of clinopyroxene crystals from the three sectors (each sector is reported in a separate panel; color legend as in Fig. 4).
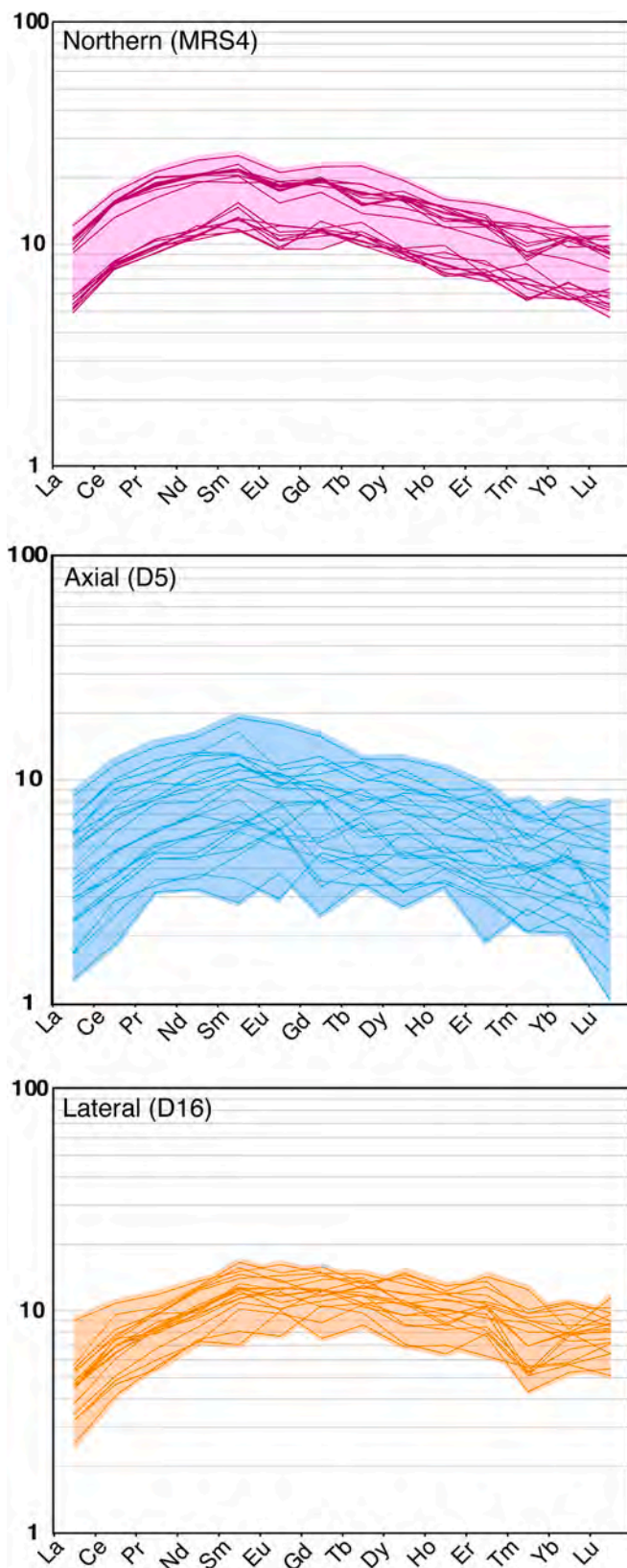
Fig. 6. Rare earth element (REE) plots normalized to CI chondrite according to McDonough and Sun (1995) for clinopyroxene crystals in basalt MRS4 from the northern sector (purple), in basalt D5 from the axial sector (blue) and in basalt D16 from lateral sector (orange). (For interpretation of the references to color in this figure legend, the reader is referred to the web version of this article.)

5. Discussion

5.1. Pre-eruptive storage conditions

Pre-eruptive storage conditions of MV magmas are evaluated by validating the results obtained using different clinopyroxene-liquid thermobarometers with the petrographic information collected on the MV lava suite. For this purpose, results from conventional thermobarometric models (Putirka, 2008; eq. 32d) are compared to results obtained using recent machine learning algorithms (Jorgenson et al., 2022), both based on the clinopyroxene-liquid equilibrium. Estimating the intensive variables that govern mineral crystallization can be challenging, particularly for rocks in which the coexisting glass is lacking due to the crystallinity of the groundmass. A commonly employed approach is to assume the whole-rock composition as representative of the silicate liquid coexisting with the mineral, assuming that chemical equilibrium exists between the two (Putirka et al., 1996). Thus, equilibrium conditions between clinopyroxene and (whole-rock) liquid composition have been tested using the model re-evaluated by Mollo et al. (2013) and built upon the early formalism introduced by Putirka et al. (1996). This model relies on the difference between observed and theoretical (i.e., predicted by regression analysis of equilibrium clinopyroxene-melt pairs) concentration of the diopside+hedenbergite component ($\Delta DiHd$) in clinopyroxene (Fig. SM3). From a theoretical point of view, equilibrium conditions are attained for absolute $\Delta DiHd$ values of <0.10 (Mollo and Masotta, 2014). As a further criterion to assess equilibrium conditions, we considered the Fe—Mg exchange between clinopyroxene and liquid [$^{cpx-melt}Kd_{Fe-Mg} = (Fe^{cpx}/Fe^{melt}) \times (Mg^{melt}/Mg^{cpx})$] (Fe calculated assuming FeO as total iron). As shown in Fig. SM3, the results are broadly consistent with the $\Delta DiHd$ test, although some clinopyroxene crystals deviate from the equilibrium range of 0.28 ± 0.08 suggested by Putirka (2008). Considered that the results of the thermobarometric modeling using only clinopyroxene crystals passing both equilibrium tests were comparable to those obtained using the entire population of clinopyroxene passing only the $\Delta DiHd$ test, this latter population was chosen for the modeling. This supports the findings of previous authors (Mollo et al., 2010; Mollo et al., 2013; Putirka, 2008) who identified the equilibrium test based on the difference between "predicted" and "measured" clinopyroxene components as a more robust test for equilibrium compared to the $^{cpx-melt}Kd_{Fe-Mg}$, due to the significant dependence of this parameter on the liquid composition.

Temperature and pressure values obtained with Jorgenson et al. (2022), using clinopyroxene-melt pairs passing the equilibrium test, were plotted in diagrams that identify the highest-probability peaks on probability tail plots (Fig. 8b), thereby indicating the more realistic estimates for the MV pre-eruptive magma storage conditions.

We compare results from different clinopyroxene-liquid thermobarometers, including the H₂O-independent eq. 32d of Putirka (2008), that yields an error of ±58 °C, and the recently developed machine learning algorithm-based model by Jorgenson et al. (2022), that yields an error of ±45 °C. In terms of temperature estimates, we observe that the model of Putirka (2008) provides realistic values for most of clinopyroxene occurring in the basaltic samples (1110–1180 °C), but it seems to largely overestimate the temperature of clinopyroxene in the andesitic samples (temperatures falling in the same range 1130–1180 °C) (Fig. SM2). On the counterpart, the model of Jorgenson et al. (2022) gives results that are shifted to lower temperatures compared to estimates obtained using the model of Putirka (2008) and spanning a much broader range (980–1080 °C). Specifically, temperature estimates obtained using the model of Jorgenson et al. (2022) discriminate the crystallization temperature of clinopyroxene in the basalt (1025–1080 °C), basaltic andesite (990–1060 °C) and andesite (930–980 °C). Note that a pressure of 200 MPa was used as input parameter to calculate clinopyroxene crystallization temperature with the model of Putirka (2008) and the pressure dependence of this model (in the order of 8 °C/kbar) does not
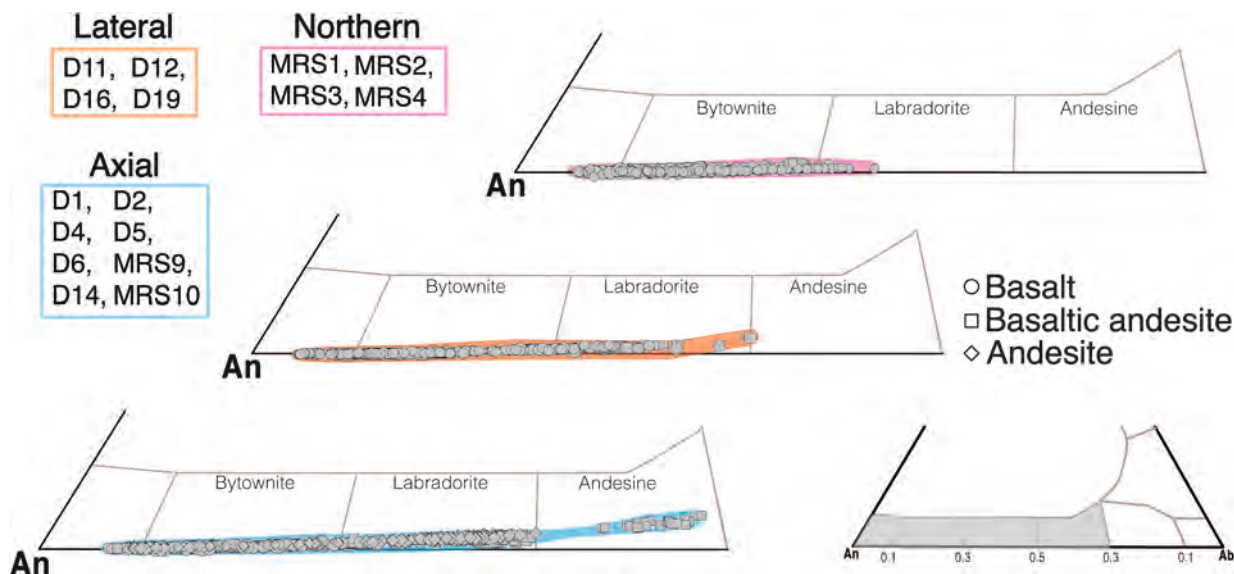
Fig. 7. Ternary diagram An-Ab-Or showing the compositional variability of plagioclase crystals from the three sectors (each sector is reported in a separate panel; color legend as in Fig. 4).
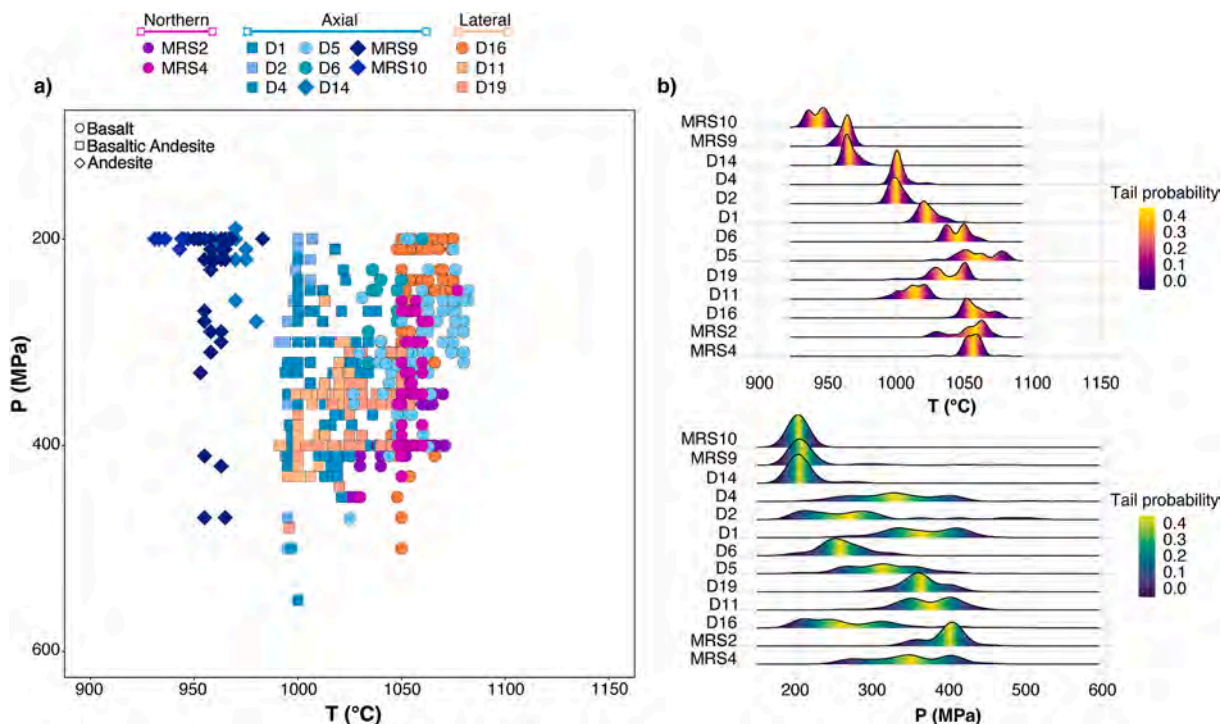

Fig. 8. (a) Pressure vs temperature estimates obtained using the machine-learning model of Jorgenson et al. (2022). (b) Tail probability plots for pressure and temperature, showing the best thermobarometric estimates for each sample. Symbol and color legend as in Fig. 4.

reconcile the inconsistency observed for the temperature estimates of the two models. Temperatures calculated with the model of Jorgenson et al. (2022) however, appear consistent with the results of thermodynamic simulations performed using Magma Chamber Simulator (MCS) (Bohrson et al., 2014, 2020; Heinonen et al., 2021; see paragraph 5.2), suggesting that these values could represent more accurately the pre-eruptive magma storage conditions.

Concerning the pressure estimates, the predictions obtained using the model of Jorgenson et al. (2022) are flattened to a minimum pressure of 200 MPa, whereas the estimates obtained using the eq. 32b of Putirka (2008) are largely scattered (Table EA3; Fig. SM2). We are

aware that due to the error associated to these models, ± 270 MPa for the model of Jorgenson et al. (2022) and ± 260 MPa for the model of Putirka (2008), it is not possible to achieve a reliable assessment of the pre-eruptive crystallization pressure of clinopyroxene from our dataset. However, we use the range of 200–400 MPa from the model of Jorgenson et al. (2022), that point to depths within the 10–12 km thick crustal column underlying MV (Manu-Marfo et al., 2019), for a comparative appraisal of clinopyroxene populations.

Fig. 8a allows us to distinguish different ranges of pressure and temperature values estimated for the lavas erupted from the different sectors of the volcano. The basaltic lavas from the northern sector

exhibit clinopyroxene crystals that record a narrower crystallization range of pressure and temperature, 280–450 MPa and 1025–1075 °C respectively. Clinopyroxene crystals from basalts and basaltic andesites from the axial sector record crystallization conditions ranging from 200 to 500 MPa, and from 1000 to 1085 °C. Clinopyroxene crystals in basalts and basaltic andesites emitted from the lateral sector record crystallization pressures ranging from 200 to 470 MPa and temperatures ranging from 990 to 1075 °C, respectively. Crystals contained in the andesitic lavas from the axial sector form a distinct cluster at a lower pressure (200 MPa) and temperature (930–980 °C) compared to basalts and basaltic andesites from other sectors (Fig. 8b).

The temperature-dependent plagioclase-liquid hygrometer proposed by Putirka (2005b) (model H, with a SEE of 1.2 wt%) has been used to evaluate the H_2O content of MV magmas. Equilibrium conditions between plagioclase and (whole-rock) liquid compositions were tested following the method discussed in Putirka (2008), based on the An-Ab exchange coefficient between mineral and melt, defined as $^{pl\text{-}melt}Kd_{Ab\text{-}An} = (XNa_{Plag} \times XAl_{liq} \times XCa_{liq})/(XCa_{Plag} \times XNa_{liq} \times XSi_{liq})$ where "liq" is the liquid composition, "Plag" is the plagioclase composition, and all components are expressed as molar fractions. According to Putirka (2008), plagioclase is defined in equilibrium with the coexisting melt if $^{pl\text{-}melt}Kd_{Ab\text{-}An} = 0.10 \pm 0.05$ at $T < 1050$ °C or 0.27 ± 0.11 at $T > 1050$ °C. As it can be observed in Table EA4, only a small portion of the plagioclase crystals satisfies the equilibrium criteria. Since the plagioclase hygrometer is temperature-dependent, we used as input values the temperatures inferred from the clinopyroxene-liquid thermo-barometer of Jorgenson et al. (2022). Owing to the higher uncertainty of temperature estimates of H_2O-dependent plagioclase-liquid thermometers (and also to avoid a circular dependence with the hygrometer), we preferred to rely on temperature values inferred from clinopyroxene. This assumption is justified by the petrographic evidence of co-saturation between clinopyroxene and plagioclase in all the investigated samples. The estimated water contents are reported in Table EA4. As illustrated in Fig. 9, the H_2O content ranges from 2 to 4 wt% and no significant differences are observed in lavas erupted from the three different sectors of the MV.
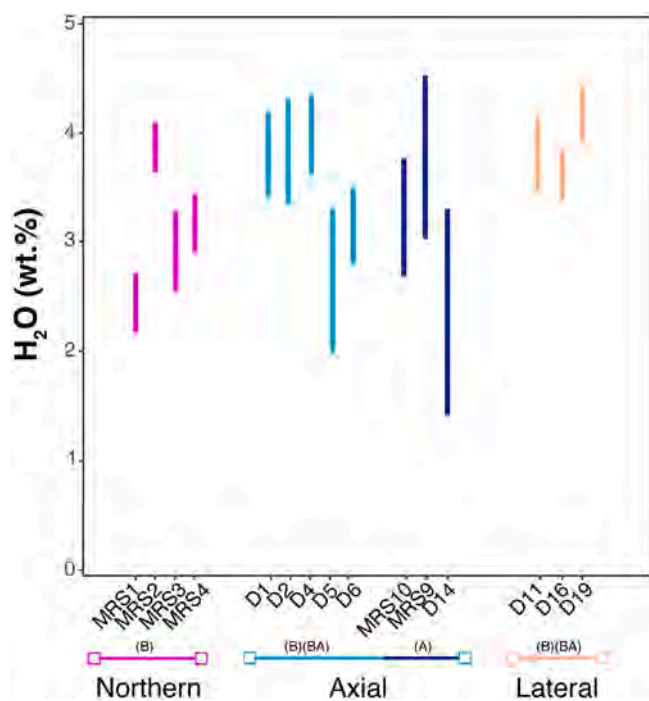

Fig. 9. H_2O estimates of magmas erupted from MV obtained using the plagioclase-liquid hygrometer (model H) of Putirka (2005). Basalt (B), Basaltic andesite (BA), Andesite (A). Color legend as in Fig. 4.

5.2. Magma differentiation

The volcanic activity of MV is mainly characterized by basalts and basaltic andesites, with the more evolved andesites collected only from the summit cone of the volcano (Fig. 1). Various magmatic scenarios have been proposed in the literature to explain the origin of andesitic magmas, including magma differentiation by crystal fractionation, crustal assimilation or mixing between magmas with different degrees of evolution (Boettcher, 1973; DePaolo, 1981; Spera and Scruggs, 2016; Wilson, 1993). In the case of MV, the whole-rock compositions point to parent-daughter relationships between basaltic and andesitic lavas, with no evidence of assimilation of the surrounding oceanic crust (Trua et al., 2011). Simple mass balance calculations presented here support this suggestion. We used as initial and final melt composition the whole-rock analyses of the basaltic and andesitic samples D5 and MRS9, respectively, and for the fractionating mineral phases, the composition of the minerals contained in these samples. Results indicate that a melt with the chemical composition of MRS9 can be reproduced with a sum of square residual (SSR) of 0.05 after a fractionation of about 53%, of which 8% olivine, 22% clinopyroxene, 21% plagioclase and 2% spinel (Table SM1).

The relatively low crystal fraction observed in the MRS9 (10–15 area %) requires some degree of crystal-melt separation, which implies extraction of the andesitic melt from a crystal-rich domain of the shallow plumbing system. The mechanisms of crystal-melt separation have been extensively discussed in the literature by means of both numerical models (Bachmann and Bergantz, 2004; Dufek and Bachmann, 2010; Masotta et al., 2016) and experimental works (Masotta et al., 2012; Shibano et al., 2013). These studies collectively evidenced that conditions favorable to extraction of a differentiated liquid from a crystal-rich domain subsist in the range of crystallinity of 50–60%, although the lower limit may shift to even lower values in case of plagioclase-rich mineral assemblages that characterize MORB settings, owing to the capability of plagioclase to form solid crystal networks (Pan and Batiza, 2003). The 50–60% range compares well with the amount of crystal fractionation calculated by mass balance modeling to form the andesitic magma. The occurrence of ultramafic to gabbroic glomerocrysts within the MV lavas (Fig. 2) provides evidence for the existence of crystal-rich domains across the entire MV trans-crustal plumbing system, possibly formed during the long-term storage, differentiation and migration of the mantle-derived melts. These processes account for the formation of crystal-poor magmas with fractionated compositions, such as the andesite erupted at the MV summit cone (Fig. 1). The finding that clinopyroxene in the crystal-poor andesites exhibits a composition similar (yet not identical) to that of crystals carried in the D2 basaltic andesite erupted from the axial sector suggests that the andesitic magmas were likely produced by a shallow level fractionation stage from a parental (D2-like) basaltic andesitic magma (Trua and Marani, 2021). Thermobarometric results with tail probability plots suggesting lower pressure and temperature crystallization conditions for clinopyroxene crystals in the andesite (Fig. 8b), further support this hypothesis.

In order to reconstruct the liquid line of descent of MV magmas, we employed the energy-constrained thermodynamic model MCS (Bohrson et al., 2014, 2020; Heinonen et al., 2021). Simulations were performed in fractional crystallization mode only and we used the basalt D5 as starting composition for the simulations, as previously done for the mass balance calculation. Several fractional crystallization paths were simulated at 100, 200 and 350 MPa and at different initial melt-H_2O contents (0, 1, 2 and 4 wt%) and temperature decrement steps of 5 °C, ensuring to embrace the whole crystallization conditions of MV. Since MCS allows running simulations only with few fixed fO_2 conditions, we calculated the Fe_2O_3 and FeO values for each normalized input composition using the model of Kress and Carmichael (1991) at the specified oxygen buffers we needed (QFM, QFM + 1 and QFM + 2) and used these normalized values as input parameters to run the simulations. For trace element, we used MCS phase-equilibria and mineral-melt partition

coefficients (Kd) for basaltic melts selected from the literature (see Table EA6 for Kd values and related references). MCS simulations yield andesitic melts in the temperature range 900–980 °C, corresponding to fractionation values of 65–55% that are comparable to the results obtained with the mass balance calculations (Table SM1). All input parameters and results of MCS simulations performed are reported in Table EA6. All simulations performed with an initial H_2O content of 2 wt % and at different pressure and fO_2 conditions reveal evolutionary paths of the residual melt that broadly achieve the major and trace element composition of the targeted andesitic samples MRS9, MRS10 and D14 (Figs. 10 and SM4). Based on the best match between the predicted liquid compositions and whole-rock analyses, we determine the best correspondences at temperatures below 970 °C in the simulations performed at 200 MPa (sample MRS9) and 350 MPa (samples MRS10 and D14), with initial fO_2 conditions corresponding to QFM to QFM + 1. It is worth noting that the temperature value of 970 °C is consistent with the estimates for the andesitic magma obtained using the clinopyroxene thermobarometer of Jorgenson et al. (2022), thereby validating the results of the machine-learning algorithm. The only crucial ambiguity arises for TiO_2 and, to a lesser extent for FeO_{tot}, whose concentrations in the residual melt are always underestimated (Fig. 10). This is due to the

fact that, within the temperature range of 1000–1020 °C, an additional ferromagnesian phase crystallizes, resembling an Al-rich (up to 18 wt%) and Ti-rich (up to 13 wt%) clinopyroxene, depleting the residual melt in TiO_2. Yet, clinopyroxene with this composition is not observed in the products of MV. Rare calcic amphibole (magnesiohastingsite) crystals are in turn hosted in the D2 axial basaltic lava (Trua et al., 2014). These crystals have lower TiO_2 (3–4 wt%) and Al_2O_3 (9–13 wt%) contents than the clinopyroxene obtained from the MCS modeling, suggesting that amphibole may take part to the crystal fractionation process as ferromagnesian phase.

5.3. Magma pathways of the MV plumbing system

The diversity in textural features and mineral chemistry observed in the sampled MV eruptive products can be interpreted considering the different pathways followed by magmas ascending through the MV feeding system. It is worth stressing the large depth range of the sampling sites, which are separated by a distance of about ~50 km, from the deep northern sector (2700–3100 m b.s.l.) to the lateral and axial sectors (2300–2500 m b.s.l and 600–1500 m b.s.l., respectively) (Fig. 1). In such a scenario, it is likely to expect that magmas erupted from the axial
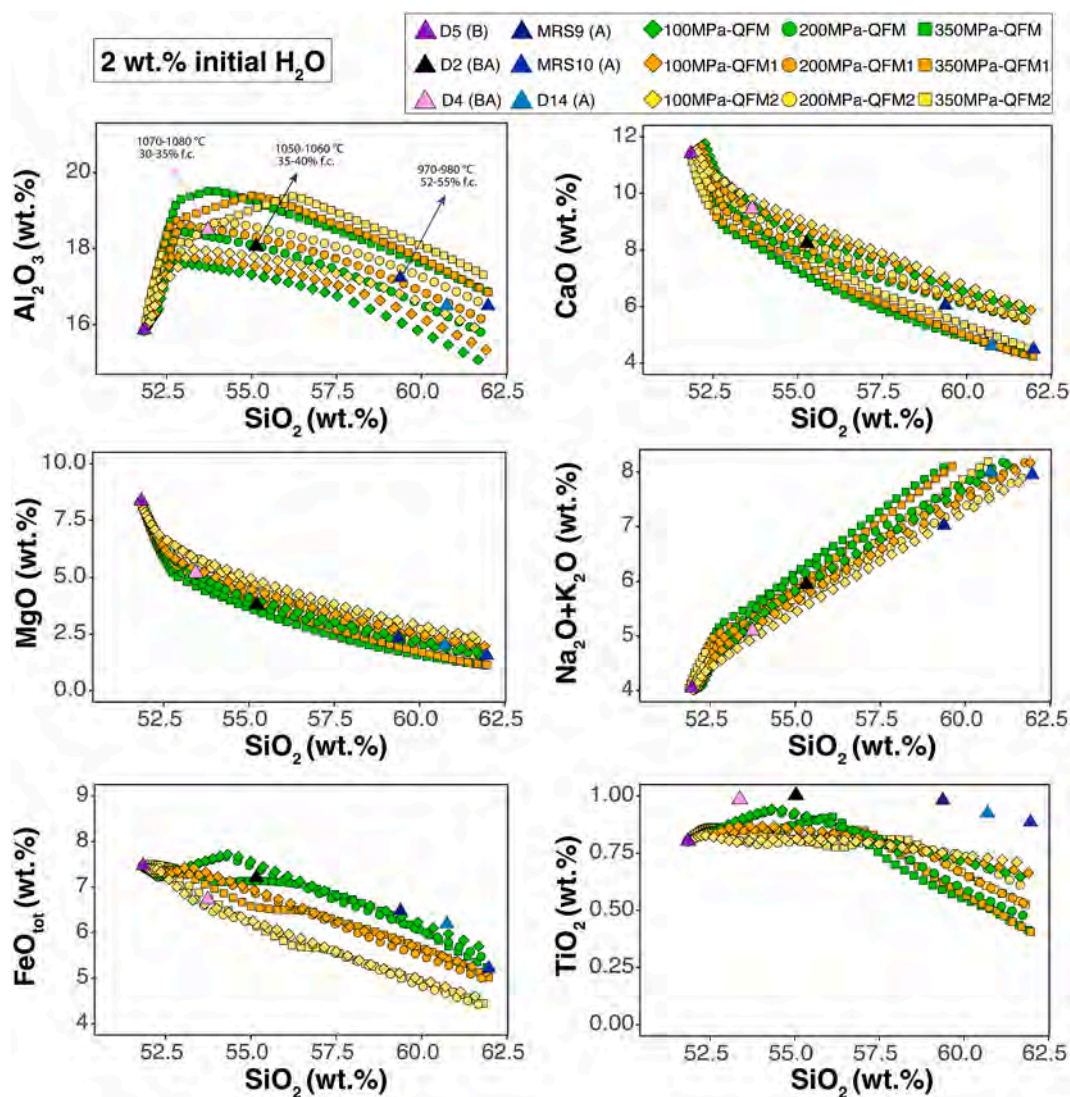

Fig. 10. Liquid line of descent calculated using Magma Chamber Simulator (Bohrson et al., 2014, 2020; Heinonen et al., 2021). Only the results of simulations performed with 2 wt% of initial H_2O content are reported, which are found to be the best match with the composition of natural whole-rocks (reported as filled triangles). The arrows indicate the approximate temperature and fractionated crystals (f.c.) at given points of the simulated differentiation paths. See text for further details.

sector experienced a protracted and more complex crystallization history compared to magmas erupted from the northern sector. Not coincidentally, samples collected from the axial sector exhibit a broader variability in terms of whole-rock compositions (from basalt to andesite), crystal content (from 15 to 30 area%) and chemical composition (see Figs. 4, 5 and 7, and previous sections), compared to the low porphyritic basalts collected from the northern sector (Fig. 2). Olivine crystals contained in basalts erupted from the northern sector are also generally more forsteritic compared to crystals contained in lavas from the other sectors (Fig. 4), testifying to a generally lower degree of differentiation experienced by magmas erupted in this sector. A similar conclusion can be drawn from the chemical variability of clinopyroxene across the different sectors, with crystals from the northern sector being slightly more enriched in MgO and with their population resulting compositionally more homogeneous, compared to crystals from the axial and lateral sectors (Figs. 3c and 5).

The chemical variability of clinopyroxene can also provide information on magma dynamics and conduit processes, as recently shown for open conduit systems (Colle et al., 2023; Giacomoni et al., 2016; MacDonald et al., 2022; Masotta et al., 2020; Pontesilli et al., 2019; Ubide and Kamber, 2018). Under certain variations in the physico-chemical conditions of the magma, clinopyroxene may undergo rapid growth, incorporating elements from the melt in abundances that deviate from that expected at equilibrium (Mollo and Hammer, 2017). Recent experimental works pointed out how the incorporation of incompatible and slow-diffusing cations in clinopyroxene lattice is more favored upon transition from an interface-limited to a diffusion-limited growth regime (Colle et al., 2023; Masotta et al., 2020; Pontesilli et al., 2019). This phenomenon extends beyond major elements, encompassing trace elements as well, with the uptake of REE in the M2 site of clinopyroxene being favored at increased concentration of ^{T}Al via charge-balancing substitutions (Ubide et al., 2019a). The transition between growth regimes and, consequently, the incorporation of slow-diffusing elements such as ^{T}Al and Ti, is normally related to an increased degree of undercooling (ΔT), defined as the difference between the liquidus temperature of the melt and the temperature at which crystallization takes place (Kirkpatrick, 1981), which is expected to occur during cooling of a magma or by degassing during ascent in the conduit.

Fig. 11 highlights that the content of incompatible cations (^{T}Al + Ti) in clinopyroxene does not decrease with increasing Mg#, as it would be expected for minerals crystallized in a less differentiated melt. Hence, considered the less evolved composition of clinopyroxene from the northern sector compared to the axial sector, the relatively higher concentrations of ^{T}Al + Ti and REE (Fig. 6) suggest that higher undercooling conditions characterized the basaltic magmas erupted from this sector. To test this hypothesis, we used the model by MacDonald et al.
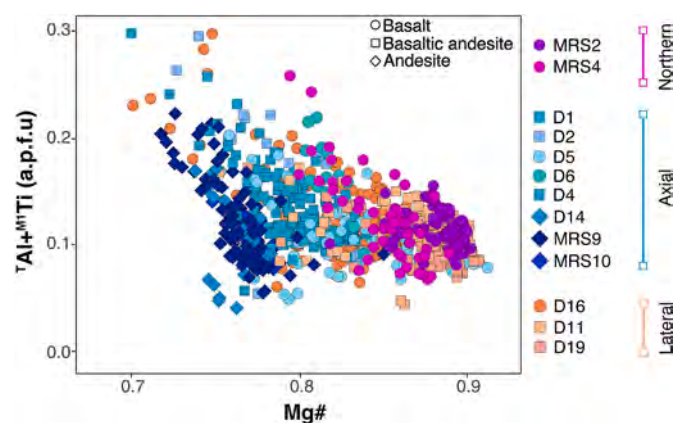

Fig. 11. Compositional diagram showing ^{T}Al + ^{M1}Ti versus Mg# variation for clinopyroxene crystals. Symbol and color legend as in Fig. 4.

(2022) based on the partition coefficient of REE between clinopyroxene and the melt (D_{REE}, calculated using the REE concentration determined in the glass; Table EA3b) to infer the ΔT conditions of clinopyroxene contained in the basaltic magmas erupted from the three sectors. The modeling returned the following values: $\Delta T = 90 \pm 39$ °C for the northern sector, $\Delta T = 30 \pm 25$ °C for the axial sector and $\Delta T = 52 \pm 27$ °C for the lateral sector. It emerges a picture where basaltic magmas erupted from the northern sector crystallized under higher regimes of undercooling compared to those erupted from the other sectors, possibly related to a more rapid ascent and a crystallization driven by a decompression-induced degassing. This hypothesis aligns with petrographic evidence such as the skeletal-dendritic forms of plagioclase and clinopyroxene in the groundmass (Fig. 3a) and the sharp compositional zoning of olivine crystals (Fig. 3b). On the other hand, the lower degree of undercooling recorded by clinopyroxene in the basaltic magmas erupted in the axial sector testifies to a prolonged residence in the crust that consistently favored the production of andesitic melts. This interpretation is also supported by the higher abundance and petrographic diversity of glomerocrysts in basaltic samples from the axial sector (Fig. 2b) and with the broader chemical variability of their minerals (Figs. 5 and 6). In this frame, ΔT values recorded by clinopyroxene from the lateral sector, comprised between those obtained for the northern and axial sectors, correlate well with the petrochemical attributes of the lateral sample D16, showing features that are intermediate between samples from the two other sectors. A general model of MV plumbing system that summarizes the observation presented in this study is reported in Fig. 12. This model illustrates how magmas *en route* to the surface move and evolve across the three distinct sectors, showing how the petrographic evidence, combined with thermobarometric constraints and thermodynamic modeling, allows to depict a scenario of the physico-chemical evolution of magmas in a back-arc volcanic setting.

6. Conclusions

We present new petrographic and chemical data obtained on lava samples from the Marsili volcano (MV), collected by dredging in the northern, axial and lateral sectors of the submarine volcanic edifice. We found that the petrologic diversity of the lava samples investigated here, together with the petrochemical data available from previous studies, permits to depict a picture of the MV trans-crustal plumbing system. Our conclusions can be summarized as follows:

1. lavas erupted from the three different sectors of the MV (northern, axial, and lateral) exhibit distinct petrological features reflective of different pathways taken by magmas *en route* to the surface;
2. the chemistry of olivine (Fo$_{83-90}$) and clinopyroxene (Mg# = 80–90) of the low porphyritic basalts erupted from the northern sector highlights a generally lower degree of differentiation of magmas compared to the basaltic magmas erupted from the axial and lateral sectors;
3. based on the relative enrichment of ^{T}Al + Ti and REE in clinopyroxene crystals, different undercooling (ΔT) conditions were inferred for magmas erupted from the northern ($\Delta T = 90 \pm 39$ °C), axial ($\Delta T = 30 \pm 25$ °C) and lateral ($\Delta T = 52 \pm 27$ °C) sectors;
4. andesitic magmas formed beneath the axial sector and at relatively shallow depths (200 MPa) were likely generated from basaltic magmas that stagnated and fractionated at pressure conditions (350 MPa) corresponding to the local Moho.

Collectively, these new data reinforce previous observations concerning the complexity of MV and allow to define a broader scenario, in which the architecture of the plumbing system has a major control on magma dynamics. Nonetheless, our knowledge of the MV system remains still preliminary, considered the heterogeneity of the crystal-rich domains inferred from the crystal cargo of the MV lavas. Future petrochemical and geochronological investigations targeting the
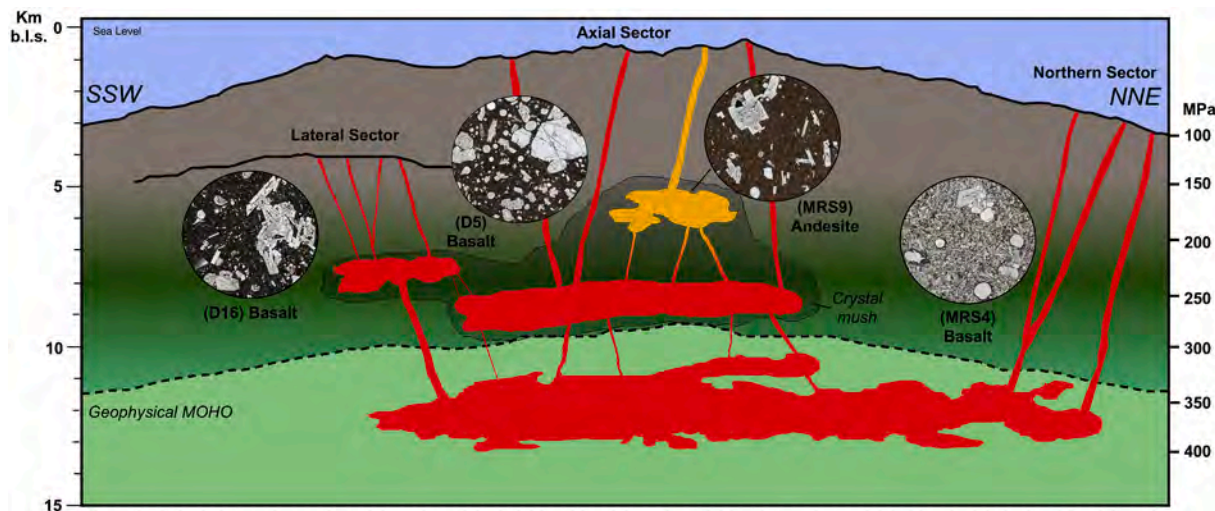
Fig. 12. Schematic representation of the plumbing system beneath the MV, highlighting diverse magma pathways for the different sectors of the volcano and related petrographic features (see text for a detailed discussion). Basaltic magmas are interpreted to be sourced from magma storage zones located at deep crustal levels, whereas andesitic magmas (erupted only from the axial summit sector) are fed from shallower storage zones. Storage depth calculated using pressure estimates and assuming a density value of $2.9*10^3$ kg/m^3. The oceanic crust that lies beneath the MV is 10–12 km-thick (Manu-Marfo et al., 2019). Relief of the MV obtained from the contours of the map in Fig. 1.

glomerocryst-rich lavas could provide an invaluable opportunity for constraining magmatic processes involved in the formation of a trans-crustal plumbing system at an active back-arc spreading center.

CRediT authorship contribution statement

Fabio Colle: Conceptualization, Data curation, Formal analysis, Investigation, Methodology, Project administration, Supervision, Writing – original draft, Writing – review & editing. **Matteo Masotta:** Conceptualization, Funding acquisition, Methodology, Supervision, Writing – review & editing. **Simone Costa:** Conceptualization, Investigation, Methodology, Writing – review & editing. **Pier Paolo Giacomoni:** Conceptualization, Methodology, Writing – review & editing. **Teresa Trua:** Conceptualization, Funding acquisition, Investigation, Methodology, Writing – review & editing. **Michael Marani:** Funding acquisition, Methodology, Writing – review & editing.

Declaration of competing interest

The authors declare that they have no known competing financial interests or personal relationships that could have appeared to influence the work reported in this paper.

Appendix A. Supplementary data

Supplementary data to this article can be found online at https://doi.org/10.1016/j.lithos.2024.107675.

References

Albert, H., Trua, T., Fonseca, J., Marani, M.P., Gamberi, F., Spiess, R., Marzoli, A., 2022. Time scales of open-system processes in a complex and heterogeneous mush-dominated plumbing system. Geology 50, 869–873.

Bachmann, O., Bergantz, G.W., 2004. On the origin of crystal-poor rhyolites: extracted from batholithic crystal mushes. J. Petrol. 45, 1565–1582.

Beier, C., Bach, W., Turner, S., Niedermeier, D., Woodhead, J., Erzinger, J., Krumm, S., 2015. Origin of silicic magmas at spreading centres - an example from the South East Rift, Manus Basin. J. Petrol. 56, 255–272.

Bennet, E.N., Lissenberg, C.J., Cashman, K., 2019. The significance of plagioclase textures in mid-ocean ridge basalt (Gakkel Ridge, Artic Ocean). Contrib. Mineral. Petrol. 174, 49.

Boettcher, A.L., 1973. Volcanism and orogenic belts – the origin of andesites. Tectonophysics 17, 223–240.

Bohrson, W.A., Spera, F.J., Ghiorso, M.S., Brown, G.A., Creamer, J.B., Mayfield, A., 2014. Thermodynamic model for energy-constrained open-system evolution of crustal magma bodies undergoing simultaneous recharge, assimilation and crystallization: the magma chamber simulator. J. Petrol. 55, 1685–1717.

Bohrson, W.A., Spera, F.J., Heinonen, J.S., Brown, G.A., Scruggs, M.A., Adams, J.V., Takach, M.K., Zeff, G., Suikkanen, E., 2020. Diagnosing open-system magmatic processes using the Magma Chamber Simulator (MCS): part I-major elements and phase equilibria. Contrib. Mineral. Petrol. 175, 1–29.

Boschetty, F.O., Ferguson, D.J., Cortés, J.A., Morgado, E., Ebmeier, S.K., Morgan, D.J., Romero, J.E., Parejas, C.S., 2022. Insights into magma storage beneath a frequently erupting Arc Volcano (Villarrica, Chile) from unsupervised machine learning analysis of mineral compositions. Geochem. Geophys. Geosyst. 23 e2022GC010333.

Burchardt, S., Annen, C.J., Kavanagh, J.L., Hazim, S.H., 2022. Developments in the study of volcanic and igneous plumbing systems: outstanding problems and new opportunities. Bull. Volcanol. 84, 59.

Burns, D.H., de Silva, S.L., Shane, P., Coble, M.A., 2022. Crustal Forensics at Pūtauaki (Mt. Edgecumbe), New Zealand reveal the influence of deep crustal arc processes on magma evolution in the Taupo Volcanic Zone. Contrib. Mineral. Petrol. 177, 16.

Cashman, K.V., Sparks, R.S.J., Blundy, J.D., 2017. Vertically extensive and unstable magmatic systems: a unified view of igneous processes. Science 355, 6331.

Colle, F., Masotta, M., Costa, S., Mollo, S., Landi, P., Pontesilli, A., Peres, S., Mancini, L., 2023. Effect of undercooling on clinopyroxene crystallization in high K basalt: implications for magma dynamics at Stromboli volcano. Lithos 456-457, 107327.

DePaolo, D.J., 1981. Trace element and isotopic effects of combined wallrock assimilation and fractional crystallization. Earth Planet. Sci. Lett. 53, 189–202.

Dufek, J., Bachmann, O., 2010. Quantum magmatism: Magmatic compositional gaps generated by melt-crystal dynamics. Geology 38, 687–690.

Gallotti, G., Zaniboni, F., Pagnoni, G., Romagnoli, C., Gamberi, F., Marani, M.P., Tinti, S., 2021. Tsunamis from prospected mass failure on the Marsili submarine volcano flanks and hints for tsunami hazard evaluation. Bull. Volcanol. 83, 2.

Gamberi, F., Marani, M., Landuzzi, V., Magagnoli, A., Penitenti, D., Rosi, M., Bertagnini, A., Di Roberto, A., 2006. Sedimentologic and volcanologic investigation of the deep Tyrrhenian Sea: preliminary result of cruise VST02. Ann. Geophys. 49, 2/3.

Geiger, H., Troll, V.R., Jolis, E.M., Deegan, F.M., Harris, C., Hilton, D.R., Freda, C., 2018. Multi-level magma plumbing at Agung and Batur volcanoes increases risk of hazardous eruptions. Sci. Rep. 8, 10547.

Gennaro, E., Iezzi, G., Cocchi, L., Ventura, G., 2023. Large silicic magma chambers at the Moho depth characterize the multi-level plumbing system of back-arc spreading ridges. Lithos 456, 107325.

Giacomoni, P.P., Ferlito, C., Coltorti, M., Bonadiman, C., Lanzafame, G., 2014. Plagioclase as archive of magma ascent dynamics on "open conduit" volcanoes: the 2001-2006 eruptive period at Mt. Etna. Earth Sci. Rev. 138, 371–393.

Giacomoni, P.P., Coltorti, M., Bryce, J.G., Fahnestock, M.F., Guitreau, M., 2016. Mt. Etna plumbing system revealed by combined textural, compositional, and thermobarometric studies in clinopyroxenes. Contrib. Mineral. Petrol. 171, 1–15.

Heinonen, J.S., Iles, K.A., Heinonen, A., Fred, R., Virtanen, V.J., Bohrson, W.A., Spera, F. J., 2021. From Binary mixing to magma chamber simulator: geochemical modeling of assimilation in magmatic systems. In: Crustal Magmatic System Evolution: Anatomy, Architecture, and Physico-Chemical Processes, Vol. 7, pp. 151–176.

Howell, D., Griffin, W.L., Pearson, N.J., Powell, W., Wieland, P., O'Reilly, S.Y., 2013. Trace element partitioning in mixed-habit diamonds. Chem. Geol. 355, 134–143.

Iezzi, G., Caso, C., Ventura, G., Vallefuoco, M., Cavallo, A., Behrens, H., Mollo, S., Paltrinieri, D., Signanini, P., Vetere, F., 2014. First documented deep submarine explosive eruptions at the Marsili Seamount (Tyrrhenian Sea, Italy): a case of historical volcanism in the Mediterranean Sea. Gondwana Res. 25 (2), 764–774.

Iezzi, G., Lanzafame, G., Mancini, L., Behrens, H., Tamburrino, S., Vallefuoco, M., Passaro, S., Signanini, P., Ventura, G., 2020. Deep sea explosive eruptions may be not so different from subaerial eruptions. Sci. Report. 10, 6709.

Jeanvoine, A., Chazot, G., Labanieh, S., Pelleter, E., Fouquet, Y., 2021. Origin and evolution of the Fatu Kapa magmatic system (North-Western Lau Back-Arc Basin): insight on the genesis of high-silica lavas. J. Petrol. 62, egab039.

Jerram, D.A., Dobson, K.J., Morgan, D.J., Pankhurst, M.J., 2018. The petrogenesis of magmatic systems: using igneous textures to understand magmatic processes. In: Volcanic and Igneous Plumbing Systems, pp. 191–229.

Jorgenson, C., Higgins, O., Petrelli, M., Bégué, F., Caricchi, L., 2022. A machine learning-based approach to clinopyroxene thermobarometry: model optimization and distribution for use in earth sciences. J. Geophys. Res. Solid Earth 127 e2021JB022904.

Kahl, M., Chakraborty, S., Pompilio, M., Costa, F., 2015. Constraints on the nature and evolution of the magma plumbing system of Mt. Etna Volcano (1991-2008) from a combined thermodynamic and kinetic modelling of the compositional record of minerals. J. Petrol. 56, 2025–2068.

Kastens, K.A., Mascle, J., 1990. The geological evolution of the Tyrrhenian Sea: an introduction to the scientific results of ODP Leg 107. In: Proceedings of the Ocean Drilling Program, Scientific Results, Vol. 107, p. 26.

Kirkpatrick, R.J., 1981. Kinetics of crystallization of igneous rocks. In: Kinetics of Geochemical Processes. De Gruyter, pp. 321–398.

Kress, V.C., Carmichael, I.S., 1991. The compressibility of silicate liquids containing Fe 2 O 3 and the effect of composition, temperature, oxygen fugacity and pressure on their redox states. Contrib. Mineral. Petrol. 108, 82–92.

Lormand, C., Zellmer, G.F., Sakamoto, N., Ubide, T., Kilgour, G., Yurimoto, H., Palmer, A., Németh, K., Iizuka, Y., Moebis, A., 2021. Shallow magmatic processes revealed by cryptic microantecrysts: a case study from the Taupo Volcanic Zone. Contrib. Mineral. Petrol. 176, 97.

MacDonald, A., Ubide, T., Mollo, S., Masotta, M., Pontesilli, A., 2022. Trace element partitioning in zoned clinopyroxene as a proxy for undercooling: experimental constraints from trachybasaltic magmas. Geochim. Cosmochim. Acta 336, 249–268.

Manu-Marfo, D., Aoudia, A., Pachhai, S., Kherchouche, R., 2019. 3D shear wave velocity model of the crust and uppermost mantle beneath the Tyrrhenian basin and margins. Sci. Rep. 9, 1–10.

Marani, M.P., Gamberi, F., Casoni, L., Carrara, G., Landuzzi, V., Musacchio, M., Penitenti, D., Rossi, L., Trua, T., 1999. New rock and hydrothermal samples from the southern Tyrrhenian Sea: the MAR-98 research cruise. Giorn. Geol. 61, 3–24.

Marani, M.P., Trua, T., 2002. Thermal constriction and slab tearing at the origin of a superinflated spreading ridge: Marsili volcano (Tyrrhenian Sea). J. Geophys. Res. Solid Earth 107, 2188.

Masotta, M., Freda, C., Gaeta, M., 2012. Origin of crystal-poor, differentiated magmas: insights from thermal gradient experiments. Contrib. Mineral. Petrol. 163, 49–65.

Masotta, M., Mollo, S., Gaeta, M., Freda, C., 2016. Melt extraction in mush zones: the case of crystal-rich enclaves at the Sabatini Volcanic District (Central Italy). Lithos 248-251, 288–292.

Masotta, M., Pontesilli, A., Mollo, S., Armienti, P., Ubide, T., Nazzari, M., Scarlato, P., 2020. The role of undercooling during clinopyroxene growth in trachybasaltic magmas: insights on magma decompression and cooling at Mt. Etna volcano. Geochim. Cosmochim. Acta 268, 258–276.

McDonough, W.F., Sun, S.S., 1995. The composition of the Earth. Chem. Geol. 120, 223–253.

Merle, R., Caroff, M., Girardeau, J., Cotten, J., Guivel, C., 2005. Segregation vesicles, cylinders, and sheets in vapor-differentiated pillow lavas: examples from Tore-Madeira rise and Chile Triple Junction. J. Volcanol. Geotherm. Res. 141, 109–122.

Mollo, S., Del Gaudio, P., Ventura, G, Iezzi, G., Scarlato, P., 2010. Dependence of clinopyroxene composition on cooling rate in basaltic magmas: implications for thermobarometry. Lithos 118 (3), 302–312.

Mollo, S., Putirka, K., Misiti, V., Soligo, M., Scarlato, P., 2013. A new test for equilibrium based on clinopyroxene-melt pairs: clues on the solidification temperatures of Etnean alkaline melts at post-eruptive conditions. Chem. Geol. 352, 92–100.

Mollo, S., Masotta, M., 2014. Optimizing pre-eruptive temperature estimates in thermally and chemically zoned magma chambers. Chem. Geol. 368, 97–103.

Mollo, S., Hammer, J., 2017. Dynamic crystallization in magmas. E. M. U. Notes Mineral 16, 373–418.

Mollo, S., Pontesilli, A., Moschini, P., Palummo, F., Taddeucci, J., Andronico, D., Del Bello, E., Scarlato, P., 2022. Modeling the crystallization conditions of clinopyroxene crystals erupted during February–April 2021 lava fountains at Mt. Etna: implications for the dynamic transfer of magmas. Lithos 420, 106710.

Morimoto, N., 1988. Nomenclature of pyroxenes. Mineral. Petrol. 39, 55–76.

Nicotra, E., Passaro, S., Ventura, G., 2024. The formation and growth mechanisms of young back-arc spreading ridges from high-resolution bathymetry: the Marsili Seamount (Tyrrhenian Sea, Italy). Geosci. Front. 15 (1), 101723.

Pan, Y., Batiza, R., 2003. Magmatic processes under mid-ocean ridges: a detailed mineralogic study of lavas from East Pacific rise 9° 30′ N, 10° 30′ N, and 11° 20′ N. Geochem. Geophys. Geosyst. 4, 11.

Paton, C., Hellstrom, J., Paul, B., Woodhead, J., Hergt, J., 2011. Iolite: Freeware for the visualisation and processing of mass spectrometric data. J. Anal. At. Spectrom. 26, 2508–2518.

Pontesilli, A., Masotta, M., Nazzari, M., Mollo, S., Armienti, P., Scarlato, P., Brenna, M., 2019. Crystallization kinetics of clinopyroxene and titanomagnetite growing from a trachybasaltic melt: new insights from isothermal time-series experiments. Chem. Geol. 510, 113–129.

Putirka, K.D., 2005. Igneous thermometers and barometers based on plagioclase+ liquid equilibria: tests of some existing models and new calibrations. Am. Mineral. 90, 336–346.

Putirka, K.D., 2008. Thermometers and barometers for volcanic systems. Rev. Mineral. Geochem. 69, 61–120.

Putirka, K., Johnson, M., Kinzler, R., Longhi, J., Walker, D., 1996. Thermobarometry of mafic igneous rocks based on clinopyroxene-liquid equilibria, 0–30 kbar. Contrib. Mineral. Petrol. 123, 92–108.

Shibano, Y., Sumita, I., Namiki, A., 2013. A laboratory model for melting erosion of a magma chamber roof and the generation of a rhythmic layering. J. Geophys. Res. Solid Earth 118, 4101–4116.

Spera, F., Scruggs, M., 2016. Fractional crystallization and assimilation. In: White, W.M. (Ed.), Encyclopedia of Geochemistry. Springer International Publishing Switzerland.

Tamburrino, S., Vallefuoco, M., Ventura, G., Insinga, D.D., Sprovieri, M., Tiepolo, M., Passaro, S., 2015. The proximal marine record of the Marsili Seamount in the last 7 ka (Southern Tyrrhenian Sea, Italy): implications for the active processes in the Tyrrhenian Sea back-arc. Glob. Planet. Chang. 133, 2–16.

Trua, T., Serri, G., Marani, M.P., Renzulli, A., Gamberi, F., 2002. Volcanological and petrological evolution of Marsili Seamount (southern Tyrrhenian Sea). J. Volcanol. Geotherm. Res. 114, 441–464.

Trua, T., Serri, G., Marani, M.P., 2007. Geochemical features and geodynamic significance of the southern Tyrrhenian backarc basin. In: Cenozoic Volcanism in the Mediterranean Area, Vol. 418, pp. 221–233.

Trua, T., Clocchiatti, R., Schiano, P., Ottolini, L., Marani, M., 2010. The heterogeneous nature of the Southern Tyrrhenian mantle: evidence from olivine-hosted melt inclusions from back-arc magmas of the Marsili seamount. Lithos 118, 1–16.

Trua, T., Marani, M.P., Gamberi, F., 2011. Magmatic evidence for African mantle propagation into the southern Tyrrhenian backarc region. In: Volcanism and Evolution of the African lithosphere, Vol. 478, p. 307.

Trua, T., Marani, M., Barca, D., 2014. Lower crustal differentiation processes beneath a back-arc spreading ridge (Marsili seamount, Southern Tyrrhenian Sea). Lithos 190, 349–362.

Trua, T., Marani, M.P., Gamberi, F., 2018. Magma plumbing system at a young back-arc spreading center: the Marsili volcano, Southern Tyrrhenian Sea. Geochem. Geophys. Geosyst. 19, 43–59.

Trua, T., Marani, M.P., 2021. Clinopyroxene crystals in basic lavas of the Marsili Volcano chronicle early magmatic stages in a back-arc transcrustal mush system. Geosciences 11, 159.

Ubide, T., Kamber, B.S., 2018. Volcanic crystals as time capsules of eruption history. Nat. Commun. 9, 326.

Ubide, T., Mollo, S., Zhao, J.X., Nazzari, M., Scarlato, P., 2019a. Sector-zoned clinopyroxene as a recorder of magma history, eruption triggers, and ascent rates. Geochim. Cosmochim. Acta 251, 265–283.

Ubide, T., Caulfield, J., Brandt, C., Bussweiler, Y., Mollo, S., Di Stefano, F., Nazzari, M., Scarlato, P., 2019b. Deep magma storage revealed by multi-method elemental mapping of clinopyroxene megacrysts at Stromboli volcano. Front. Earth Sci. 7, 239.

Vasey, D.A., Cowgill, E., Cooper, K.M., 2021. A preliminary framework for magmatism in modern continental back-arc basins and its application to the Triassic-Jurassic tectonic evolution of the Caucasus. Geochem. Geophys. Geosyst. 22, 6.

Weber, G., Caricchi, L., Arce, J.L., 2020. The long-term life-cycle of Nevado de Toluca Volcano (Mexico): insights into the origin of petrologic modes. Front. Earth Sci. 8, 563303.

Wilson, M., 1993. Magmatic differentiation. J. Geol. Soc. Lond. 150, 611–624.

Woodhead, J.D., Hellstrom, J., Hergt, J.M., Greig, A., Maas, R., 2007. Isotopic and elemental imaging of geological materials by laser ablation inductively coupled plasma-mass spectrometry. Geostand. Geoanal. Res. 31, 331–343.

Zitellini, N., Ranero, C.R., Loreto, M.F., Ligi, M., Pastore, M., D'Oriano, F., Valenti, S., Grevemeyer, I., Moeller, S., Prada, M., 2019. Recent inversion of the Tyrrhenian Basin. Geology 48, 123–127.